MNRAS **000**, 1–9 (2025) Preprint 3 September 2025 Compiled using MNRAS LATEX style file v3.2

Snow, Soot, and Rock Lines: Equilibrium Chemistry and Transport near the Dead Zone Inner Boundary - Kavli Summer Program in Astrophysics Report

Arturo Cevallos Soto[1]*
[1]*Department of Physics and Astronomy, University of Nevada, Las Vegas, 4505 S. Maryland Pkwy, Las Vegas, NV, 89154, USA*

3 September 2025

ABSTRACT

We investigate how inward pebble drift and gas advection reshape inner–disk chemistry in the context of Inside–Out Planet Formation (IOPF). Using a 1-D midplane model that couples LTE equilibrium compositions from GGchem to operator–split advection of gas and drift of $a_p = 1$ cm pebbles, we follow an evolutionary sequence in which the accretion rate decays from $\dot{m} \sim 10^{-8}$ to $10^{-9}\ M_\odot\ \mathrm{yr}^{-1}$ over 10^5 yr. As the disk cools, the H_2O snowline migrates inward and a co–moving enrichment ridge forms in water vapor. Interior to the front, gas–phase H_2O increases by nearly two orders of magnitude within 10^5 yr. Elementally, O/H rises strongly near and inside the migrating water front, whereas C/H stays close to its initial value (owing to the absence of a solid carbon reservoir), producing a deep, snowline–locked trough in gas and total C/O that propagates inward. Early-time oxygen released at rock-lines provides a secondary inner contribution. The modeled inner disk therefore becomes increasingly O-rich and H_2O-dominated inside ∼1 au, consistent with some emerging observations of water-rich inner regions. However, at the current state of the model, while the snowline and the rock-line are clearly visible, the soot-line is not discernible.

Key words: protoplanetary discs – astrochemistry – planets and satellites: formation

1 INTRODUCTION

NASA's Kepler mission revealed that Systems with Tightly-packed Inner Planets (STIPs) are common, straining "form-far, migrate-in" narratives of planet assembly. Inside-Out Planet Formation (IOPF) offers a contrasting, in-situ pathway in which planets assemble sequentially from pebble-rich rings that are continuously fed by inward-drifting solids (see overview by Tan et al. 2016). Early in disk evolution, magnetorotational instability (MRI) is active in a disk's midplane inward of $\sim$ 0.1–1 au (set primarily by the contemporaneous accretion rate), while an MRI-inactive "dead zone" occupies larger radii. The pressure maximum at the Dead Zone Inner Boundary (DZIB) traps the inward-migrating solid particles ("pebbles"), allowing a dense ring to form and collapse into a protoplanet (e.g., Hu et al. 2015; Cai et al. 2022). Once sufficiently massive, the body perturbs the gas, opens a gap, and pushes the pressure maximum outward by several Hill radii, resetting the trap and enabling the next ring–planet cycle.

Concurrently, the disk's physical and chemical states evolve (e.g., Walsh et al. 2010, 2015; Booth et al. 2017; Booth & Ilee 2019). Gas participates in high-temperature gas-phase chemistry while also exchanging material with dust via freeze-out and grain-surface reactions; ice mantles on grains host additional chemistry that can build complex organic molecules. Dust itself grows by coagulation and mantle accretion, settles toward the midplane, and increasingly decouples from the gas, promoting rapid radial drift. These aerodynamically coupled pebbles deliver volatile ices from the cold outer disk into warmer regions; upon crossing their respective ice lines, the different ices sublimate and enrich the local gas, catalyzing further processing (e.g., Booth et al. 2017; Booth & Ilee 2019; Molyarova et al. 2021). In parallel, advective inflow of gas steadily resupplies inner disk material near the DZIB. Given Myr-scale disk lifetimes, the combined action of pebble drift and gas advection can substantially reshape the composition of both solids and gas available to growing planets.

Observationally, several disks show inner regions that are oxygen-rich (water-rich) in the warm molecular layer. Using Spitzer and ALMA samples, Banzatti et al. (2020) found that mid-IR H_2O line luminosities anti-correlate with the outer mm-dust radius, which they interpret as evidence that efficient inward drift of icy pebbles replenishes inner-disk water, yielding O-rich chemistry. Recent JWST/MIRI results now resolve and extend this picture with, for example, protoplaneray disk Sz 98 showing abundant inner water and a possibly C/O ratio below unity in contrast with the rest of the disk (Gasman et al. 2023), and SY Cha revealing water enhancements linked to a disk substructure that modulates the delivery of ice-coated pebbles (e.g., Schwarz et al. 2024).

A second relevant boundary to inner disk C/O ratios is the "soot-line" (also called the "tar line"), which is the sublimation/destruction front of solid-state carbon carriers like amorphous carbon, refractory organics, and polycyclic hydrocarbons (PAHs). Inside this boundary, at midplane conditions $T \sim$ 500–700 K, carbonaceous grains are irreversibly destroyed or volatilized, driving carbon into the gas (see e.g., Lodders 2004; Kress et al. 2010). The soot-line moves inward as disks cool, regulating the carbon budget of inner planetesimals and providing a natural pathway to Earth's measured carbon deficit, while

---

* E-mail: cev.arturo@gmail.com

© 2025 The Authors

formation between the soot and snow lines can yield carbon-rich solids with implications for atmospheric hazes and bulk compositions (see e.g., Li et al. 2021; Bergin et al. 2023).

At yet higher temperatures than the volatile ice- and soot-lines, the very inner disk hosts also rock-lines, where refractory solids (silicates and oxides) sublimate. The dust sublimation front sets the hot inner rim at $T \sim 1500$ K (depending on composition, size, and gas–density), a location and morphology that are now well constrained by near-IR interferometry and modeling of the curved, “puffed-up”, inner rim (see e.g., Isella & Natta 2005; Dullemond & Monnier 2010). In the same way, as the disk cools, this evaporation front migrates inward, with thermally driven opacity/pressure transitions around it possibly creating additional local gas-pressure maxima that concentrate and modulate migration of remaining solids, and formation pathways (see e.g., Vinković 2012; Morbidelli et al. 2016; Flock et al. 2019).

Prior modeling has already done on this topic. Midplane studies by Eistrup et al. (2016, 2018) employed detailed gas-grain networks to track time-dependent chemistry, showing that cosmic-ray-induced and surface processes can drive outer-disk ice reservoirs toward H_2O and CO_2 dominance, with initial abundances imprinting long-lived effects (including on C/O in gas and ice). However, these calculations neglected dynamical transport and grain growth. Conversely, Booth et al. (2017); Booth & Ilee (2019) coupled chemistry to gas advection and pebble drift, demonstrating that inward-migrating pebbles can strongly condition inner-disk abundances by releasing ices at their snowlines. However, those works used a reduced chemical network, limiting the breadth of species and pathways that could be explored, and ignored the chemistry of the refractory material.

The report is organized as follows. Section 2 presents the midplane’s structure, transport prescriptions, and thermo-chemical equilibrium code, along with the scheme used to couple chemistry and flow. Section 3 reports the evolving volatile budgets for the prototype model, and other derived quantities (elemental ratios and C/O ratio in gas and solids), while pointing out important features. Section 4 summarizes our work and outlines further improvements and goals for the continued development of this work-in-progress model.

2 METHODS

2.1 Disk physical properties

We model the midplane of a geometrically thin, steady α–disk (Shakura & Sunyaev 1973, see), consistent with prior IOPF studies (Chatterjee & Tan 2014; Hu et al. 2018, see). Here heating is dominated by viscous dissipation in the inner, active region and by stellar irradiation in the outer, passive region. The disk is specified by the accretion rate $\dot{m}$, stellar properties, and viscosity parameter α. The local thermodynamic and dynamical quantities follow Hu et al. (2018):

$$T = T(r) \tag{1}$$

$$c_s(r) = (\gamma k_B T/\mu)^{1/2} \tag{2}$$

$$h(r)/r = c_s/v_K \tag{3}$$

$$\nu(r) = \alpha c_s h \tag{4}$$

$$\Sigma_g(r) = \dot{m}/(3\pi\nu) \tag{5}$$

$$\rho(r) = \Sigma_g/(h\sqrt{2\pi}), \tag{6}$$

with $\gamma = 1.4$, $P = K\rho^{\gamma}$, k_B Boltzmann’s constant, $\mu = 2.33$, $m_H = 3.90 \times 10^{-24}$ g, h the scale height, v_K the Keplerian speed, ν the kinematic viscosity, Σ_g the gas surface density, and ρ the midplane gas volumetric density. Unless otherwise noted we adopt a Sun-like star with $m_* = 1\,M_\odot$, $r_* = 3\,R_\odot$, $T_* = 4500$ K, and $L_* = 3.3\,L_\odot$.

In the viscously heated active region, the midplane temperature obeys (Chatterjee & Tan 2014)

$$\begin{aligned} T(r) = {} & \frac{3^{1/5}}{2^{7/5}\pi^{2/5}}\left(\frac{\mu}{\gamma k_B}\right)^{1/5}\left(\frac{\kappa}{\sigma_{\rm SB}}\right)^{1/5} \\ & \times\alpha^{-1/5}(Gm_*)^{3/10}(f_r\dot{m})^{2/5}r^{-9/10}\ {\rm K} \\ & \rightarrow 290\gamma_{1.4}^{-1/5}\kappa_{10}^{1/5}\alpha_{-4}^{-1/5}m_{*,1}^{3/10}(f_r\dot{m}_{-9})^{2/5}r_{\rm au}^{-9/10}\ {\rm K}, \end{aligned} \tag{7}$$

where κ is the Rosseland-mean opacity (tabulated values from Zhu et al. 2009), $\sigma_{\rm SB}$ the Stefan–Boltzmann constant, G the gravitational constant, $f_r \equiv 1 - \sqrt{r_*/r}$, and $r_{\rm au} \equiv r/{\rm au}$. Based on Hu et al. (2018), beyond the transition where irradiation dominates, the passive midplane temperature is

$$T(r) = 172\, r_{\rm au}^{-3/7}\ {\rm K}. \tag{8}$$

The corresponding surface density profiles are

$$\begin{aligned} \Sigma_g \quad = \quad & \frac{2^{7/5}}{3^{6/5}\pi^{3/5}}\left(\frac{\mu}{\gamma k_B}\right)^{4/5}\left(\frac{\kappa}{\sigma_{\rm SB}}\right)^{-1/5} \\ \times \quad & \alpha^{-4/5}(Gm_*)^{1/5}(f_r\dot{m})^{3/5}r^{-3/5} \\ \rightarrow \quad & 880\gamma_{1.4}^{-4/5}\kappa_{10}^{-1/5}\alpha_{-4}^{-4/5}m_{*,1}^{1/5} \\ & (f_r\dot{m}_{-9})^{3/5}r_{\rm au}^{-3/5}\ {\rm g\,cm^{-2}}, \end{aligned} \tag{9}$$

for the active region, and for the passive region

$$\begin{aligned} \Sigma_g \quad = \quad & \frac{1}{516\pi}(1\ {\rm au})^{-3/7}\frac{\mu}{\gamma k_B} \\ \times \quad & \alpha^{-1}(Gm_*)^{1/2}\dot{m}r^{-15/14} \\ \rightarrow \quad & 11.2\gamma_{1.4}^{-1}\alpha_{-4}^{-1}m_{*,1}^{1/2}\dot{m}_{-9}r_{\rm 100au}^{-15/14}\ {\rm g\,cm^{-2}}. \end{aligned} \tag{10}$$

Because chemistry is sensitive to density, we also track the midplane number density of H nuclei, $n_{\rm H} = (5/3)n$ for predominantly molecular gas with $n_{\rm He} = 0.1\,n_{\rm H}$. In the active region

$$\begin{aligned} n_{\rm H} \quad = \quad & \frac{5}{3}\frac{2^{8/5}}{3^{13/10}\pi^{9/10}}\frac{\mu^{1/5}}{(\gamma k_B)^{6/5}}\left(\frac{\kappa}{\sigma_{\rm SB}}\right)^{-3/10} \\ \times \quad & \alpha^{-7/10}(Gm_*)^{11/20}(f_r\dot{m})^{2/5}r^{-33/20} \\ \rightarrow \quad & 2.43\times10^{14}\gamma_{1.4}^{-6/5}\kappa_{10}^{-3/10}\alpha_{-4}^{-7/10}m_{*,1}^{11/20} \\ & \times(f_r\dot{m}_{-9})^{2/5}r_{\rm au}^{-33/20}\ {\rm cm^{-3}}, \end{aligned} \tag{11}$$

and in the passive region

$$\begin{aligned} n_{\rm H} \quad = \quad & \frac{5}{3}\frac{1}{1032\sqrt{86}\pi^{3/2}}(1\ {\rm au})^{-9/14}\frac{\mu^{1/2}}{(\gamma k_B)^{3/2}} \\ \times \quad & \alpha^{-1}Gm_*\dot{m}r^{-6/7} \\ \rightarrow \quad & 1.11\times10^{10}\gamma_{1.4}^{-1}\alpha_{-4}^{-1}m_{*,1}^{1/2}\dot{m}_{-9}r_{\rm 100au}^{-15/14}\ {\rm cm^{-3}}. \end{aligned} \tag{12}$$

Parameter choices are guided by T Tauri statistics and MRI expectations: $\dot{m} \sim 10^{-8}$–$10^{-10}\,M_\odot\,{\rm yr}^{-1}$ and $\alpha \sim 10^{-4}$–10^{-3} in the

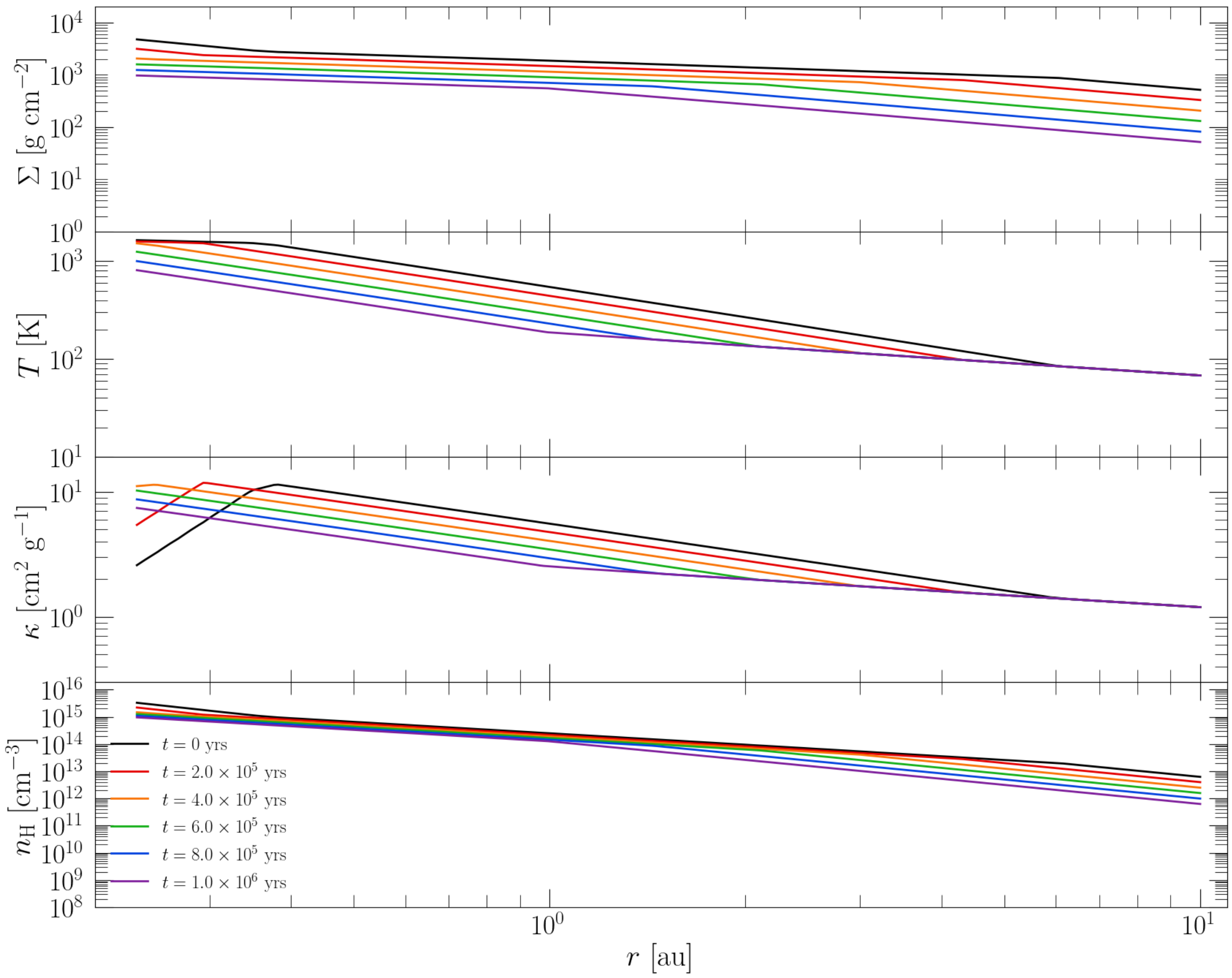

Figure 1. Radial profiles of disk properties, showing an evolutionary sequence for an exponentially decaying accretion rate from $\dot{m} = 10^{-8}\ M_\odot\ \mathrm{yr}^{-1}$ to $10^{-9}\ M_\odot\ \mathrm{yr}^{-1}$ in 10^5 years. From top to bottom, the rows show: gas mass surface density (Σ), midplane temperature (T), midplane opacity (κ), and midplane number density of H nuclei (n_H).

dead zone, rising to $\sim 10^{-2}$–0.1 where MRI is active (e.g., Alcalá et al. 2013; Manara et al. 2014; Dzyurkevich et al. 2010). Our chemistry–transport models focus on the dead zone down to the DZIB (defined by $T \simeq 1200$ K); we therefore fix $\alpha = 10^{-4}$ throughout and ignore the innermost MRI-active cavity. We consider static disks with $\dot{m} = 10^{-8}$ or 10^{-9}, $M_\odot$, yr^{-1}, and a time-evolving case with exponentially declining accretion (Bitsch et al. 2015; Hu et al. 2018),

$$\dot{m} = \dot{m}_0 e^{-t/t_0}, \tag{13}$$

with $\dot{m}_0 = 10^{-8}\ M_\odot\ \mathrm{yr}^{-1}$ and $t_0 = 4.34\times10^4$ yr (a factor of 10 decay over 10^5 yr.

Currently, the radial grid has 12 points, logarithmically spaced from $r_\mathrm{in} = 0.232$ au (the DZIB for $\dot{m} = 10^{-9}\ M_\odot\ \mathrm{yr}^{-1}$) to $r_\mathrm{out} = 10$ au. Thanks to accretion heating, for different $\dot{m}$ this inner boundary would realistically lie in different points with the passing of time; therefore, the innermost cells of the model should be interpreted cautiously since an MRI-active prescription is not included.

Figure 1 shows the radial profiles of Σ, T, κ and n_H for the aforementioned evolving accretion rate. Evolution along this sequence is the final fiducial model we will present. We note that the temperatures range from just over 1000 K in the inner regions down to about 100 K at 10 au. On the same range, the number densities range from about $n_\mathrm{H} \sim 10^{16}\ \mathrm{cm}^{-3}$ to $\sim 10^{13}\ \mathrm{cm}^{-3}$.

2.2 Gas and pebble radial velocities

Gas and solids in the midplane drift inward toward the star. The gas radial speed is

$$v_{r,g} = \frac{3\alpha}{2}\frac{c_s}{v_K}c_s, \tag{14}$$

yielding typical values of order $\sim 1\ \mathrm{cm\ s}^{-1}$ across our models.

Pebble drift is set by aerodynamic drag. Small grains are tightly coupled to the slightly sub-Keplerian gas and thus follow the gas inflow, whereas larger pebbles feel a headwind of speed v_Δ that removes angular momentum. Defining the friction time $t_\mathrm{fric} \equiv m_p v_\Delta / |F_D|$

and $\tau_{\rm fric} \equiv \Omega_K t_{\rm fric}$, the steady-state radial drift relative to the gas is

$$v_{r,p} \simeq -k_P \left(\frac{c_s}{v_K}\right)^2 \left(\tau_{\rm fric} + \tau_{\rm fric}^{-1}\right)^{-1} v_K, \qquad (15)$$

with $k_P \simeq 2.4$ for $P = P_0(r/r_0)^{-k_P}$ and $\Omega_K \equiv v_K/r$ (Armitage 2009). We compute $t_{\rm fric}$ and the appropriate drag regime following Hu et al. (2018); Epstein drag applies over most radii, while Stokes becomes relevant in the innermost disk.

Pebble drift accelerates with pebble size and is faster in lower-$\dot{m}$ disks due to reduced densities and temperatures. From calculating the drift times $t_{\rm drift} \equiv r/|v_{r,p}|$, for $\dot{m} = 10^{-8}\, M_\odot\,{\rm yr}^{-1}$ only large pebbles initially at $\lesssim 1$ au and gas inside a few fractions of an au reach the inner disk within 10^5 yr, whereas for $\dot{m} = 10^{-9}\, M_\odot\,{\rm yr}^{-1}$ solid material from farther out (~ 10 au) can contribute on the same timescale, while gas remains slow.

2.3 Chemical modeling

In each cell of our grid we utilize GGchem (see Woitke et al. 2018) to compute thermo-chemical equilibrium compositions. This code determines joint gas–condensate equilibrium by minimizing the total Gibbs free energy at given T, ρ, and bulk elemental abundances. It enforces elemental conservation and condensate stability, returning self-consistent gas-phase and condensed-phase abundances for up to 41 elements. This equilibrium framework is well-suited to the dense, hot, UV and cosmic-ray-shielded inner protoplanetary disk's midplane, where LTE is reasonably expected and reactive/condensational processes can be assumed to proceed faster than disequilibrium mechanisms (see e.g., Line et al. 2010).

For all cells we initially adopt Solar elemental nuclei number fractions, treated as conserved bulk abundances and normalized so that $\sum_i n_i = 1$. Hydrogen and helium dominate ($n_{\rm H} \simeq 0.927$, $n_{\rm He} \simeq 0.0716$), while the major rock- and volatile-forming elements (e.g., O, C, N, Mg, Si, Fe) appear at the 10^{-4}–10^{-6} level. The values used are listed in Table 1.

2.4 Combined chemical evolution and advective transport

We evolve chemistry and transport on the 1-D grid uniform in $\log r$, where each cell represents an annular ring with fixed physical conditions (gas density, temperature, etc.) set by α-disk midplane values at the cell center and vertical extent equal to the local scale height h. This defines each cell's volume and mass.

Chemistry and advection are operator-split. (i) Chemistry step: for each cell we advance abundances from t to $t + {\rm d}t$ using GGchem at the cell's fixed density and temperature. (ii) Advection step: we compute interface fluxes using gas and pebble velocities at cell boundaries. The gas flux is normalized to enforce a constant accretion rate at all radii, which we achieve by a small adjustment to the cell's inner-boundary height to reconcile the viscous $\dot{m}$ (evaluated at cell center) with the interface flux. Incoming material into a cell is assumed to mix instantaneously and completely within the receiving cell. We then update gas- and solid-phase species inventories accordingly. This transport is purely inward. Material exiting the inner boundary leaves the domain (into the unresolved innermost disk), while currently the outer boundary supplies a steady inflow that keeps its composition fixed (which is unrealistic).

The timestep ${\rm d}t$ obeys an advective CFL-like condition such that the drift distance covered by the pebbles does not exceed 0.9 of a receiving cell's radial width. In practice, the most restrictive constraint arises from rapid pebble drift in the innermost zones.

Species	**Abundance (num. frac.)**
H	9.271×10^{-1}
He	7.159×10^{-2}
Li	1.077×10^{-11}
Be	1.382×10^{-11}
B	2.305×10^{-10}
C	3.112×10^{-4}
N	8.895×10^{-5}
O	7.008×10^{-4}
F	3.279×10^{-8}
Ne	6.174×10^{-5}
Na	2.168×10^{-6}
Mg	3.588×10^{-5}
Al	2.771×10^{-6}
Si	3.992×10^{-5}
P	2.816×10^{-7}
S	1.554×10^{-5}
Cl	2.811×10^{-7}
Ar	2.183×10^{-6}
K	1.275×10^{-7}
Ca	2.176×10^{-6}
Sc	1.109×10^{-9}
Ti	1.041×10^{-7}
V	9.783×10^{-9}
Cr	4.792×10^{-7}
Mn	2.268×10^{-7}
Fe	2.231×10^{-5}
Co	8.456×10^{-8}
Ni	1.698×10^{-6}
Cu	1.372×10^{-8}
Zn	3.810×10^{-8}
Ga	7.148×10^{-10}
Ge	3.430×10^{-9}
Rb	4.373×10^{-10}
Sr	7.110×10^{-10}
Y	1.401×10^{-10}
Zr	5.463×10^{-10}
Nb	5.364×10^{-11}
Mo	1.169×10^{-10}
Ru	6.163×10^{-11}
Rh	2.421×10^{-11}
Pd	3.512×10^{-11}
Ag	1.155×10^{-11}
Cd	6.650×10^{-11}
In	4.340×10^{-11}
Sn	9.446×10^{-11}
Sb	1.023×10^{-11}
Rb	4.373×10^{-10}
Sr	7.110×10^{-10}
Y	1.401×10^{-10}
Zr	5.463×10^{-10}
W	2.711×10^{-11}

Table 1. Solar elemental nuclei number fractions (normalized to $\sum n_i = 1$) used as bulk abundances for the equilibrium calculations.

3 PRELIMINARY RESULTS AND DISCUSSION

Here we present the current results of chemically evolving the disk using the physical profiles previously presented and GGchem to solve the gas and condensation chemistry. We follow a disk that cools from $\dot{m} \sim 10^{-8}$ to $10^{-9}\, M_\odot\,{\rm yr}^{-1}$ over 10^5 yr on a 12–cell grid, using LTE equilibrium chemistry coupled to inward advection of gas and $a_p = 1$ cm pebbles. The relatively large pebble size is

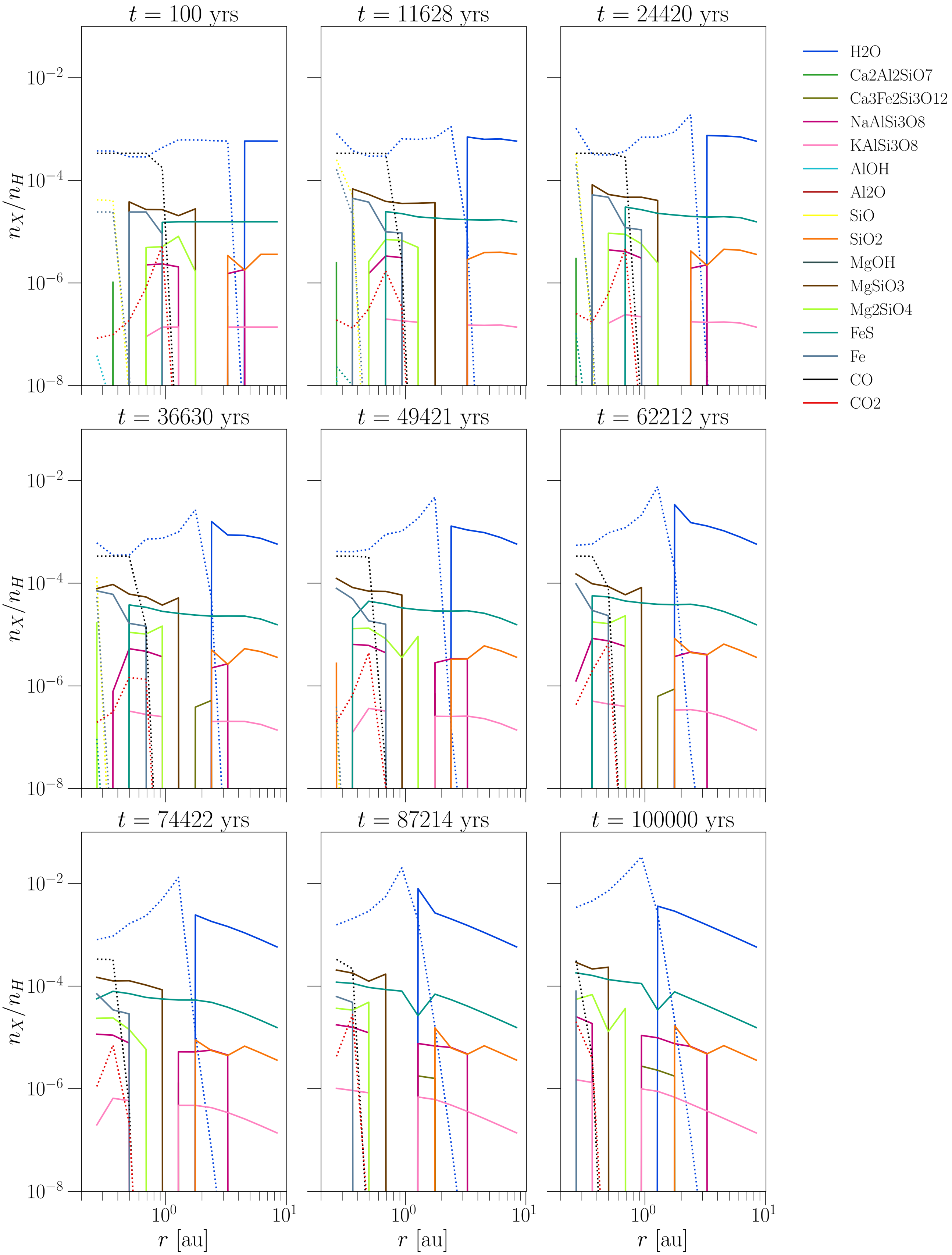

Figure 2. Radial profiles of the abundances of important key species at nine epochs up to 10^5 yr during the GGCHEM+advection run with $a_p = 1$ cm. Dotted and solid curves show gas and solid components, respectively

chosen to emphasize rapid radial drift and thus the chemical imprint of sublimation at moving snow/soot/rock lines.

In the following subsections we show evolution of common abundances, elemental ratios (C/H, O/H and N/H), and the C/O ratio.

3.1 Single pebble size chemical evolution of inner disk

Figure 2 shows nine snapshots of key species. At early times (e.g., $t = 100$–2.4×10^4 yr) the composition is close to the instantaneous equilibrium set by the hotter $\dot{m} \sim 10^{-8}$ profile. As the disk cools, the H_2O snowline migrates inward and a clear enrichment "bump" appears in the gas at each corresponding front. This bump is produced by the continuous inward supply of icy pebbles and their immediate sublimation upon crossing the local ice line, after which the released volatiles mix within the receiving cell and are partially carried further inward by the gas flow.

Water overwhelmingly dominates the inner-disk response. Between ~0.1–1 au the gas-phase H_2O abundance tracks the inward-moving H_2O snowline and builds up steadily. By $t = 10^5$ yr the peak H_2O vapor abundance interior to the front has increased by nearly two orders of magnitude relative to the initial state. This water vapor exceess appears to contribute to the enhancement of other important gas-phase species CO_2 and CO.

The figure also shows inward motion and sublimation fronts at several rock-lines, which carve sharp abundance drops in refractory species as the disk cools. There several Si, Fe, Mg, K, Ca, etc., oxygen rich, gas-phase molecules appear to rise and grow with abundance with time as the solid lines of condensed material disappear. However, it's important to note the lack of important solid-phase, carbon bearing species in this evolution picture.

3.2 Elemental C/H and O/H abundance ratios

Figure 3 tracks the radial evolution of elemental abundances (gas, solids, and their sum) for carbon and oxygen. The behavior mirrors the species trends in Fig. 2. As the disk cools and icy pebbles drift inward, the H_2O snowline sweeps inward and the local oxygen budget is steadily transferred from solids to gas. A narrow, co–moving enhancement develops in gas-phase (and therefore total) O/H at the snowline, and strengthens with time. By $t = 10^5$ yr, the peak gas–phase O/H just interior to the snowline has risen from the original $\sim 10^{-3}$ and it's on its way of reaching 10^{-1} on the entire inner region, while the solid O/H shows the corresponding depletion interior to the front and recovery exterior to it. A secondary oxygen, gas-phase rise appears deeper in, near rock sublimation fronts, where refractory oxygen carriers are released as vapor, only to later disappear as they abandon our simulation area.

In contrast, the carbon budget remains virtually unchanged in this setup. Because no substantial solid carbon reservoir is present (no solid C/H line visible), gas-phase and total C/H stay near their initial value at all radii and epochs. The total C/H is flat to mildly curved close to 1 au, probably reflecting modest CO/CO_2 redistribution. The net outcome is an increasingly O–rich inner disk: O/H rises strongly near and interior to the migrating H_2O snowline, whereas C/H remains approximately solar, setting the stage for a declining gas–phase C/O ratio inside ~1 au.

3.3 C/O ratio

Figure 4 shows that the C/O ratio responds in a highly non-linear way to the coupled drift–sublimation cycle. At early times the gas C/O is close to its initial Solar value ~ 0.43 across the modeled radii. With the rapid sublimation and mixing, the sharp raise of O/H and C/H remaining nearly unchanged, the result is a pronounced trough in gas C/O just interior to the snowline that co-moves inward with it. By $t = 10^5$ yr this trough deepens substantially and the C/O value falls well below solar in regions $\lesssim 1$ au, reflecting the sharp increase of H_2O vapor shown in Figure 2. A secondary, weaker dip can appear closer to the star when rock-line sublimation releases additional refractory oxygen to the gas before they exit the simulation area.

Because the present model contains no significant solid carbon reservoir (no soot/organic carbon component), the solid C/O remains essentially zero and there is no compensating carbon release on the inside (i.e., no "soot-line" signature). Consequently, the total C/O inherits the snowline-locked trough and also declines in the inner disk. Including a carbonaceous solid reservoir and its thermal processing would be expected to lift C/O locally near the carbon sublimation/destruction front. Its absence here explains the dramatic, monotonic drop in C/O interior to the H_2O line.

4 SUMMARY & FUTURE

In this report we presented a prototype inner–disk chemistry–transport model that couples LTE equilibrium compositions from GGchem to inward advection of gas and rapidly drifting $a_p = 1$ cm pebbles on a logarithmic 12–cell grid while the disk cools from $\dot{m} \sim 10^{-8}$ to $10^{-9}\, M_\odot\, \mathrm{yr}^{-1}$ over 10^5 yr. The coupled drift–sublimation cycle produces strong, snowline–locked enrichment of H_2O vapor that co–moves inward with the H_2O snowline. Interior to the front, the gas–phase H_2O abundance rises by nearly two orders of magnitude within 10^5 yr. Elementally, O/H increases sharply near and inside the migrating water front whereas C/H remains close to its initial value owing to the absence of a solid carbon reservoir, yielding a deep trough in the gas (and total) C/O that propagates inward with time. Additional oxygen release at rock–lines provides a secondary, inner contribution early on. Overall, the modeled inner disk becomes increasingly O–rich and water–dominated inside ~1 au, qualitatively consistent with emerging observational evidence for water–rich inner regions.

Looking ahead, several extensions are required to turn this prototype model into a predictive inner–disk chemistry and transport model.

Firstly, concerning the computation time, give that these simulations can be quite computationally expensive, we will have to parallelize the operator–split chemistry+advection loop (radial domain decomposition) to accelerate runs and enable substantially higher radial resolution, allowing us to resolve narrow enrichment fronts (snow/soot/rock lines). On the same topic of higher zone count, the inner boundary will have to be moved inward to include higher midplane temperatures to better capture rock–line chemistry.

Secondly, beyond the single–size approximation, we will explore prescribed and evolved grain size distributions and ultimately a multi–grain (multi–bin) model with size–dependent drift, sublimation/condensation, and surface–area tracking. This is necessary to study a more realistic model of grain drift.

Thirdly, the fixed–composition outer inflow has to be replaced by a more realistic supply linked to an outer–disk transport+chemistry calculation. We plan to couple the midplane LTE module to a non–LTE, time–dependent gas–grain network for the cooler/irradiated upstream regions, so that boundary abundances evolve self–consistently with the global disk.

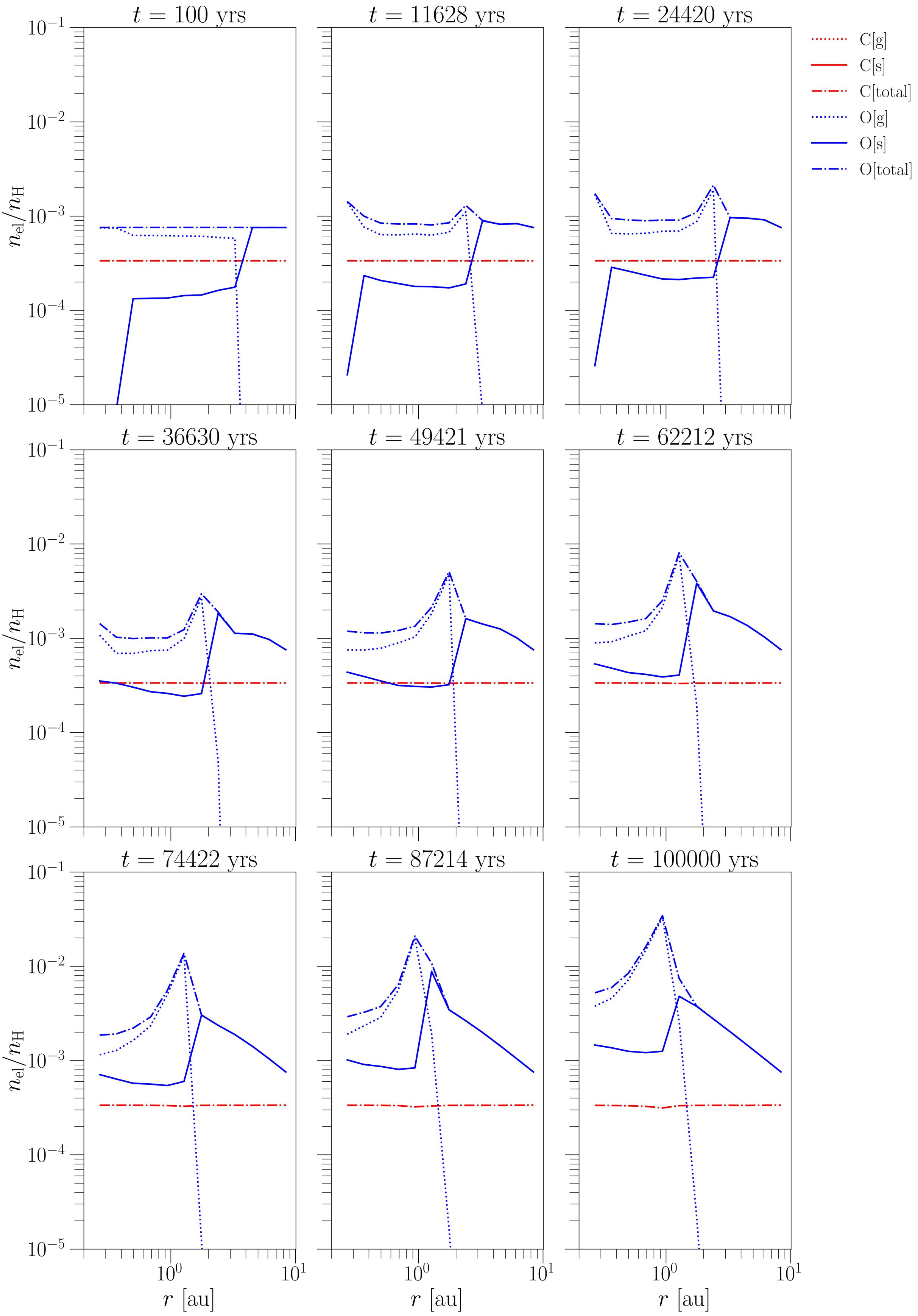

Figure 3. Radial profiles of elemental abundances at nine epochs up to 10^5 yr during the GGchem+advection run with $a_p = 1$ cm. Dotted, solid, and dash-dotted curves show gas, solid, and total components, respectively

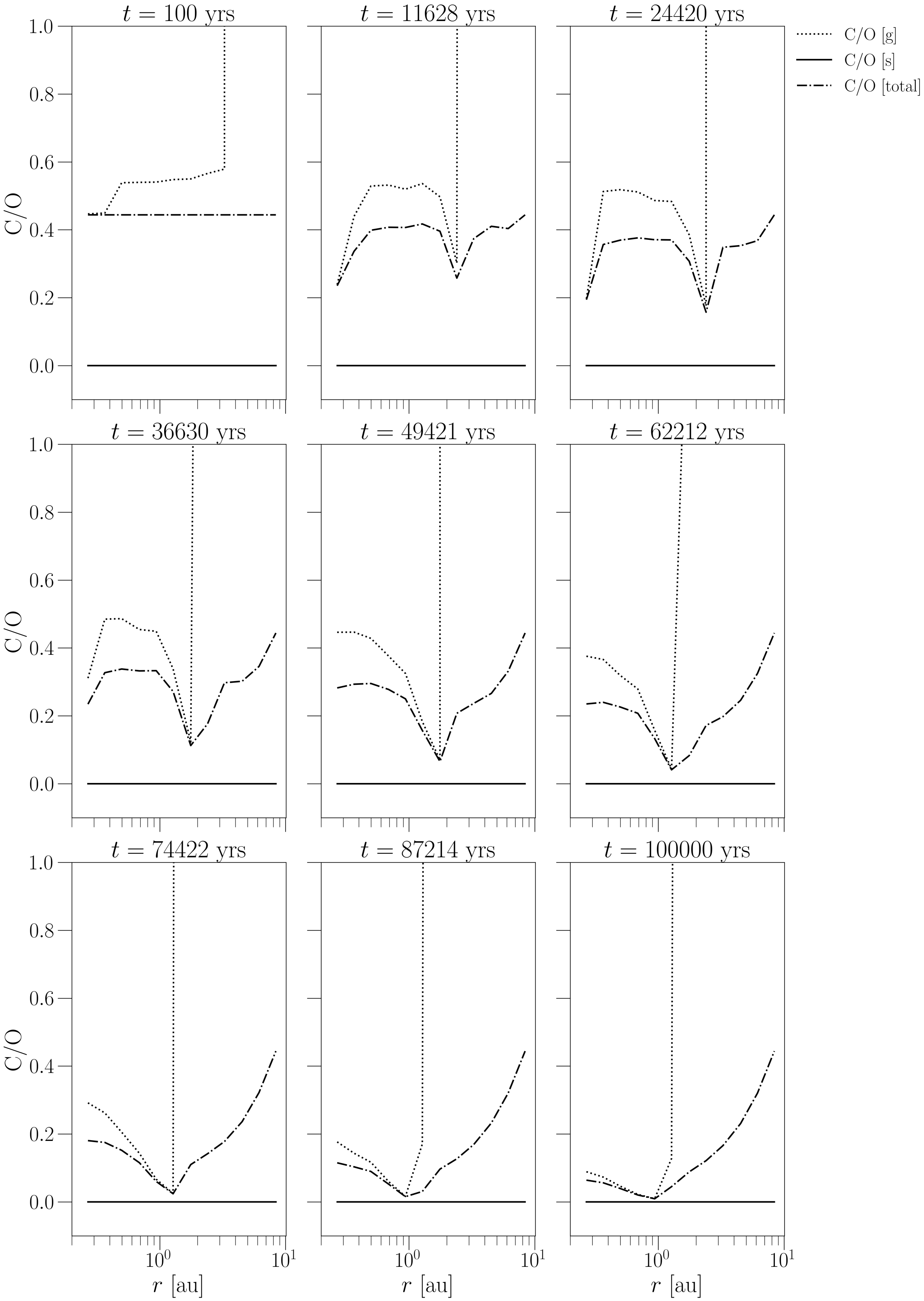

Figure 4. Radial profiles of the C/O ratio at nine epochs up to 10^5 yr during the GGchem+advection run with $a_p = 1$ cm. Dotted, solid, and dash-dotted curves show gas, solid, and total components, respectively

Fourthly, a key uncertainty is the fate of solid carbon. The current equilibrium condensation module lacks a sufficiently rich set of carbon–bearing condensates to produce a robust soot–line (if at all). The condensate list has to be expanded (e.g., amorphous C, refractory organics/CHON phases, relevant carbides/carbonates, etc.) with consistent thermochemical data and validate against canonical condensation sequences. Only then can we test whether a distinct soot–line emerges under our inner–disk conditions.

Finally, with these upgrades, we will confront the model against inner–disk O/H and C/O diagnostics and the inferred locations/motion of enrichment fronts, providing a tighter link between pebble-drift+advection and observed C/O ratios in disks.

ACKNOWLEDGEMENTS

This work originated from a project of the Summer Program in Astrophysics 2025 held at the University of Virginia, and funded by the Center for Global Inquiry and Innovation, the National Science Foundation (Grant 2452494), the National Radio Astronomy Observatory (NRAO), the Kavli Foundation and the Heising-Simons Foundation.

REFERENCES

Alcalá J. M., et al., 2013, Astronomy & Astrophysics, 561, A2
Armitage P. J., 2009, Astrophysics of Planet Formation. Cambridge University Press, doi:10.1017/CBO9780511802225
Banzatti A., et al., 2020, The Astrophysical Journal, 903, 124
Bergin E. A., Kempton E. M. R., Hirschmann M., Bastelberger S. T., Teal D. J., Blake G. A., Ciesla F. J., Li J., 2023, ApJ, 949, L17
Bitsch B., Lambrechts M., Johansen A., 2015, The growth of planets by pebble accretion in evolving protoplanetary discs (`arXiv:1507.05209`)
Booth R. A., Ilee J. D., 2019, Monthly Notices of the Royal Astronomical Society, 487, 3998–4011
Booth R. A., Clarke C. J., Madhusudhan N., Ilee J. D., 2017, Monthly Notices of the Royal Astronomical Society, 469, 3994–4011
Cai M. X., Tan J. C., Portegies Zwart S., 2022, MNRAS, 510, 5486
Chatterjee S., Tan J. C., 2014, ApJ, 780, 53
Dullemond C. P., Monnier J. D., 2010, ARA&A, 48, 205
Dzyurkevich N., Flock M., Turner N. J., Klahr H., Henning T., 2010, Astronomy & Astrophysics, 515, A70
Eistrup C., Walsh C., van Dishoeck E. F., 2016, Astronomy & Astrophysics, 595, A83
Eistrup C., Walsh C., van Dishoeck E. F., 2018, Astronomy & Astrophysics, 613, A14
Flock M., Turner N. J., Mulders G. D., Hasegawa Y., Nelson R. P., Bitsch B., 2019, A&A, 630, A147
Gasman D., et al., 2023, A&A, 679, A117
Hu X., Zhu Z., Tan J. C., Chatterjee S., 2015, The Astrophysical Journal, 816, 19
Hu X., Tan J. C., Zhu Z., Chatterjee S., Birnstiel T., Youdin A. N., Mohanty S., 2018, The Astrophysical Journal, 857, 20
Isella A., Natta A., 2005, A&A, 438, 899
Kress M. E., Tielens A. G. G. M., Frenklach M., 2010, Advances in Space Research, 46, 44
Li J., Bergin E. A., Blake G. A., Ciesla F. J., Hirschmann M. M., 2021, Science Advances, 7, eabd3632
Line M. R., Liang M. C., Yung Y. L., 2010, ApJ, 717, 496
Lodders K., 2004, ApJ, 611, 587
Manara C. F., Testi L., Natta A., Rosotti G., Benisty M., Ercolano B., Ricci L., 2014, Astronomy & Astrophysics, 568, A18
Molyarova T., Vorobyov E. I., Akimkin V., Skliarevskii A., Wiebe D., Güdel M., 2021, The Astrophysical Journal, 910, 153
Morbidelli A., et al., 2016, Icarus, 267, 368
Schwarz K. R., et al., 2024, ApJ, 962, 8
Shakura N. I., Sunyaev R. A., 1973, A&A, 500, 33
Tan J. C., Chatterjee S., Hu X., Zhu Z., Mohanty S., 2016, IAU Focus Meeting, 29A, 6
Vinković D., 2012, MNRAS, 420, 1541
Walsh C., Millar T. J., Nomura H., 2010, The Astrophysical Journal, 722, 1607–1623
Walsh C., Nomura H., van Dishoeck E., 2015, Astronomy & Astrophysics, 582, A88
Woitke P., Helling C., Hunter G. H., Millard J. D., Turner G. E., Worters M., Blecic J., Stock J. W., 2018, A&A, 614, A1
Zhu Z., Hartmann L., Gammie C., 2009, The Astrophysical Journal, 694, 1045–1055

This paper has been typeset from a TEX/LATEX file prepared by the author.